Communications in Physics, Vol. 35, No. 4 (2025), pp. 325-346
DOI: https://doi.org/10.15625/0868-3166/23002

Diverse electronic, magnetic, optical and electronic transport properties of the penta-NiN_2 nanoribbons: A first-principles investigation

Nguyen Hai Dang[1,2], **Pham Thi Bich Thao**[1], **Thai Van Thanh**[3] **and Nguyen Thanh Tien**[1,†]

[1]*College of Natural Sciences, Can Tho University, Can Tho City 94000, Vietnam*
[2]*Faculty of basic, Nam Can Tho University, Can Tho City 94000, Vietnam*
[3]*Faculty of Basic Sciences, Vinh Long University of Technology and Education, Vinh Long City 85100, Vietnam.*

E-mail: †nttien@ctu.edu.vn

Received 13 June 2025; *Accepted for publication 17 September 2025*
Published 9 December 2025

Abstract. *In this work, the structural, electronic, optical, and electronic transport properties of the p-NiN_2 nanoribbons with four typical edge shapes of armchair–armchair, sawtooth–sawtooth, zigzag–armchair, and zigzag–zigzag are fully revealed by the key quantities developed from density functional theory calculations, including the binding energies, thermal stability from ab initio molecular dynamics simulations, spin-splitting electronic band structures, atom-projected density of states, spatial spin density distribution, optical absorption spectra, I-V curves, transmission functions (T(E)), and spin filtering efficiency. As a result, all the p-NiN_2NR systems achieve a good structural stability. On the electronic characteristics, only the ZA8 configuration behaves as ferromagnetic half-metal, while other configurations all belong to ferromagnetic semiconductors. The origin of the magnetism is clarified by the spatial spin density distribution. The optical absorption spectra of the penta NiN_2 nanoribbon indicates that the absorption spectral region can be sensitively controlled by the widths and edge shapes. The I-V spectra evidences that the negative differential characteristics and the spin filtering efficiency appear in the DAA7, DSS7, and DZA6 configurations, and only disappear in the DZZ7 configuration. The transmission function (T(E)) of the DAA7-up and the DSS7-up configurations shows stronger negative differential effect than that of the the DZA6-up and DZZ7-up configurations. In addition, the spin filtering efficiency (SFE) of the DAA7 and DSS7 configurations are much higher than that of the DZA6 and DZZ7 configurations. The essential electronic, optical, and electronic transport properties of the p-NiN_2 nanoribbons controlled by edge shapes and widths are very potential for next-generation electronic, optoelectronic, and spintronic applications.*

Keywords: Penta-NiN_2 nanoribbons; DFT calculation; HSE06 functional; electronic structure; spin density distribution; optical absorption spectra; electronic transport characteristics.

Classification numbers: 31.15.A; 73.63.-b; 75.75.-c.

1. Introduction

Up to now, a large number of 2D layered materials with pentagonal structures have been studied theoretically by density functional theory (DFT), molecular dynamics (MD) simulations, Monte Carlo simulations, and machine learning (ML) to predict and assess the stability of them [1–6]. The calculation results show that pentagonal 2D materials (penta-2DMs) possess several key properties that set them apart from other 2D materials [7–12]. Specifically, the most defining characteristic of penta-2DMs is their pentagonal arrangement of atoms, forming a Cairo tessellation. This unique arrangement leads to inherent anisotropy, so penta-2DMs exhibit direction-dependent electronic, optical, and mechanical properties for specialized applications that require directional control of properties. Some penta-2DMs display negative Poisson's ratios from their buckled structures and bond configurations are suitable for applications in sensors, actuators, and impact-resistant materials [13–16]. Additionally, unlike graphene's zero bandgap, most penta-2DMs are semiconductors with finite bandgaps, making them suitable for electronic and opto-electronic applications. In addition, many penta-2DMs exhibit high air stability, making them more practical for real-world applications. In particular, the successful synthesis of $PdSe_2$, PdPS, PdPSe, NiN_2, and penta-silicon nanoribbons has opened up great potential for the search for new materials with diverse applications [17–21].

A combination of crystal-chemical design and high-pressure synthesis, Bykov and co-workers demonstrate the existence of p-NiN_2 pentagonal Cairo tessellation possessing atomic-thick layers featuring [18]. Contrasting with the bulk material's metallic behavior, p-NiN_2 exhibits elastic anisotropy and a tunable direct band gap expanding its applications in various fields. NiN_2 doped with various transition metals has potential applications for bifunctional catalytic activity for both oxygen evolution reaction (OER) and oxygen reduction reaction due to their low over-potentials [22]. The Ir embedded NiN_2 monolayer exhibits high-efficiency OER catalysts [23]. Calculation results using DFT have demonstrated that penta-NiN_2 is suitable for sodium-ion batteries (NIBs) and potassium-ion batteries (KIBs) due to high ion storage capacity, low diffusion energies, low average open-circuit voltage, strong adsorption capacity and good electronic conductivity compared to many other 2D electrode materials [24]. In particular, NiN_2/NiN_2 and Graphene/NiN_2 heterostructures have potential for use in lithium-ion batteries (LIBs). However, NiN_2/NiN_2 heterostructures have more advantages such as higher theoretical capacity, fast lithium diffusion, minimum deformation, enhanced electrochemical activity, improved structural stability, and higher charge transfer which are suitable for high-capacity and fast-charging applications [25]. Penta-NiN_2 with high adsorption energy, high sensitivity and lower operational voltage has also shown promising sensing performance, especially for NO and NO_2, compared to existing sensors like graphene, phosphorene, MoS_2, and penta-graphene [26]. Potential applications in nanoelectronics and optoelectronic devices due to their tunable properties under strain of penta NiN_2 have also been investigated.

Moreover, the unique electronic properties of pentagonal 1D materials arise from their specific atomic structure, which includes a combination of sp^2 and sp^3 hybridized atoms, and the way they are cut from penta-materials sheets. Different edge terminations (zigzag, armchair, or saw-tooth) result in different electronic behaviors, making them potentially useful in nanoelectronic devices [27–30].

The successful experimental synthesis and the diverse application potentials from the theoretical results indicate that penta NiN_2 deserves further detailed study, especially for the one-dimensional penta NiN_2 structures. The richness of edge shapes and widths of the one-dimensional penta structures promises to provide a comprehensive picture of this penta structure. Therefore, in this study, four basic edge shapes with widths ranging from 5 to 15 of penta NiN_2 nanoribbons (p-NiN_2NRs) were selected to study the stability, electronic properties, optical properties and electron transport phenomena using density functional theory combined with nonequilibrium Green's function theory.

The rest of this work is organized as follows: in Section 2 we give a brief description of the methodology of the study in this work, while in Section 3 the main results are presented and discussed. Finally in Section 4 we draw out conclusions.

2. Methodology

The 4 typical edge shapes, including sawtooth–sawtooth (SS), armchair–armchair (AA), zigzag–armchair (ZA), and zigzag–zigzag (ZZ) of the p-$PdSe_2$NR structure are formed by cutting the 2D p-$PdSe_2$NR in different directions. To eliminate the dangling bonds, hydrogen atoms are passivated at the edges of the four nanoribbon forms. First, the structural stability of the 20 different relaxed configurations of AA, SS, ZA, and ZZ with ribbon widths ranging from 5 to 15 is evaluated by the binding energies using the following formula:

$$E_B = \frac{E_{\mathtt{total}} - n_{\mathtt{Ni}}E_{\mathtt{Ni}} - n_{\mathtt{N}}E_{\mathtt{N}} - n_{\mathtt{H}}E_{\mathtt{H}}}{n_{\mathtt{Ni}} + n_{\mathtt{N}} + n_{\mathtt{H}}}. \tag{1}$$

In Eq. (1), the binding energy of studied structures, the ground-state energy of the total system, the ground-state energy of isolated Ni, N, and H systems are denoted E_B (eV/atom), $E_{\mathtt{total}}$, $E_{\mathtt{Ni,N,H}}$ (eV), respectively. The numbers of nickel, nitrogen and hydrogen atoms in the unit cell are described by $n_{\mathtt{Ni,N,H}}$.

In this study, to enhance the accuracy in calculating the bandgaps and optical quantities, the HSE06 approach in Atomistix ToolKit (ATK) package [31] are used. The calculations utilized PseudoDojo pseudopotentials and a linear combination of atomic orbitals (LCAO) basis set [32]. The studied 1D ribbon structures are periodic along the z-direction that the confinement occurs in x and y-directions, whereas the vacuum spaces set at 15 Å to avoid the interaction with nearest neighbor images. The density mesh cutoff was set to 1500 eV for both optimization and self-consistent calculations. Meanwhile, the k-points set at $1 \times 1 \times 35$ and $1 \times 1 \times 200$ for the optimal and self-consistent calculations, respectively, while the 0.001 eV/Å and 10^{-6} eV are the convergence values of the force and energy set during calculations.

The optical absorption coefficient of the materials is determined by [33]

$$\alpha = \frac{2\omega\kappa}{c}, \tag{2}$$

where, c is the velocity of light in vacuum and extinction coefficient κ

$$\kappa = \sqrt{\frac{\sqrt{\varepsilon_1^2 + \varepsilon_2^2}}{2} - \frac{\varepsilon_1}{2}}. \tag{3}$$

ε_1 and ε_2 are the real and imaginary parts of the dielectric function

$$\varepsilon(\omega) = \varepsilon_1(\omega) + i\varepsilon_2(\omega), \tag{4}$$

ω is the angular frequency of the incident photon.

Among the investigated nanoribbons, the four structures of AA7, SS7, ZA6, and ZZ7 are selected to construct the device consisting of semi-infinite left electrode (L), semi-infinite right electrode (R), and central scattering region (C). The spin-dependent current through the system is determined by the Landauer-Büttiker formula [34, 35]

$$I(V_b) = \frac{e}{h}\int_{\mu_R}^{\mu_L} \{T_\sigma(E,V_b)[f_L(E,V_b) - f_R(E,V_b)]\}\, dE, \tag{5}$$

e and h are the electron charge and the Planck's constant, respectively. $f_{L,R}(E,V_b)$ is the Fermi distribution functions of the electronic carriers in the leads, and $\mu_{L,R}$ is the electrochemical potentials of the left and right leads. $T_\sigma(E,V_b)$ is defined as follows

$$T_\sigma(E,V_b) = Tr\left[\mathrm{Im}\left\{\sum_{L\sigma}^{r}(E,V_b)\right\} G_\sigma^r(E,V_b) \times \mathrm{Im}\left\{\sum_{L\sigma}^{r}(E,V_b)\right\} G_\sigma^a(E,V_b)\right]. \tag{6}$$

Equation (6) allows to determine the transmission of an electron with spin (σ), energy (E) at bias voltage (V_b) with the retarded (advanced) Green's function matrix denoted by G^r and (G^a), respectively.

3. Results and discussion

3.1. Structural properties

The optimal geometric structures under top view projection of the p-NiN_2NRs with the twenty different configurations within H-passivated edges are displayed in Fig. 1, whereas the widths of the studied configurations are made of from 5 to 15 dimer lines along y-direction. These optimal configurations will be utilized for further investigating in their electronic, optical, and electronic transport properties.

To evaluate the structural stability of the studied configurations, their binding energies are calculated as resulted in Fig. 2, in which the binding energies show significant negative values in the range of -6.1 to -7.0 eV. These significant negative values indicate the good stability of p-NiN_2NRs. These bingding energies decrease with increasing widths, meaning that p-NiN_2NRs are more stable with the increased widths. Comparing the binding energies of four different edge shapes, the SS-p-NiN_2 possess the lowest binding energies, followed by the ZZ-p-NiN_2, ZA-p-NiN_2, and AA-p-NiN_2, as displayed by the red, magenta, blue, and black lines in Fig. 2, respectively. This is consistent with that of the reported penta graphene nanoribbon (PGNR), whereas the SS-PGNR is the most stable, while the AA-PGNR is the least stable [11]. As for the modification in structural parameters, the bond lengths at the two edges of all studied structures do not differ significantly. However, it can be clearly seen that the displacement of hydrogen atoms from the structural plane in each edge shape of p-NiN_2NRs is different, especially, for the ZZ edge shape. This may lead to diversity in the fundamental properties of the studied structures [36, 37]. Furthermore, the Fig. 3 presents a comprehensive evaluation of thermal stability for the four distinct nanoribbon configurations (AA7, SS7, ZA6, and ZZ7), assessed via ab initio molecular dynamics

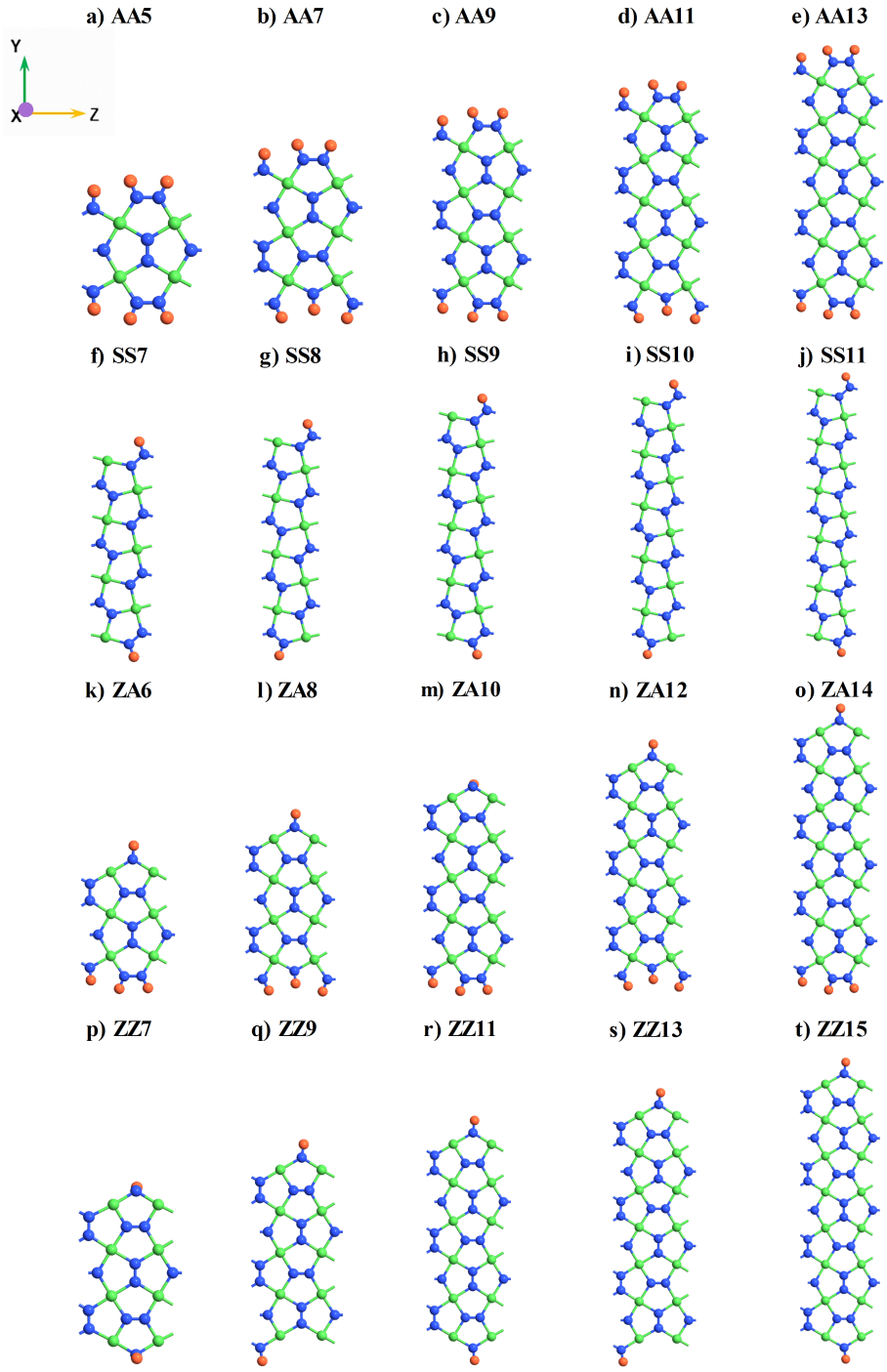

Fig. 1. Top-view model of the p-NiN_2NRs with 20 optimal configurations for four edge types. The green, blue, and orange balls represent Ni, N and H atoms, respectively.

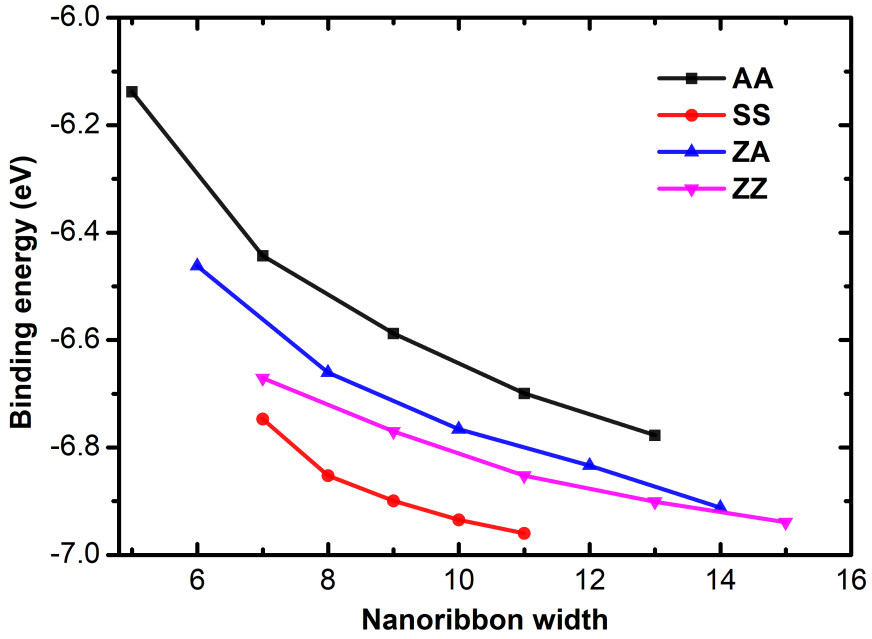

Fig. 2. (Color online) Binding energy plotted as a function of the nanoribbon width for the four edge types of p-NiN_2NRs.

(AIMD) simulations conducted over an extended period of 10,000 steps (timestep 0.5 fs). For all four cases, the total energy exhibits only minor fluctuations well within a narrow range of approximately 0.5 eV around a constant average value. This behavior is a clear hallmark of systems that have successfully reached and maintained thermal equilibrium. Crucially, this remarkable stability in energy serves as compelling evidence that the initial atomic geometries were preserved throughout the simulation, with no bond-breaking events or significant structural deformations observed.

3.2. Electronic and optical properties

The bandgap of penta NiN_2 nanoribbons varies with edge shapes and widths as shown in Fig. 4 as well as reported Table 1 and Table 2. Specifically, the AA-p-NiN_2 structures exhibit ferromagnetic semiconducting behavior that the bandgaps of both spin up (black line) and spin down (red line) decrease as their widths increase, and the bandgaps of the spin up are larger than that of the spin down, as displayed in Fig. 4(a). For the bandgaps of the SS-p-NiN_2 structures shown in Fig. 4(b), the variation in bandgap for the spin up (black line) and spin down (red line) are different, in which the bandgaps of the spin down decrease as its widths increase. In contrast, the bandgap variation of the spin up is nonlinear, which the highest and smallest bandgaps occur at the SS8 and SS7 structures, respectively. Besides, the bandgaps of the spin down are larger than that of spin up, regardless of any widths. The nonlinear bandgap variation remains in the ZA-p-NiN_2 structures as shown in Fig. 4(c), in which the highest and smallest bandgaps of spin up are at the ZA10 and ZA8 structures, respectively, while the highest and smallest bandgaps of

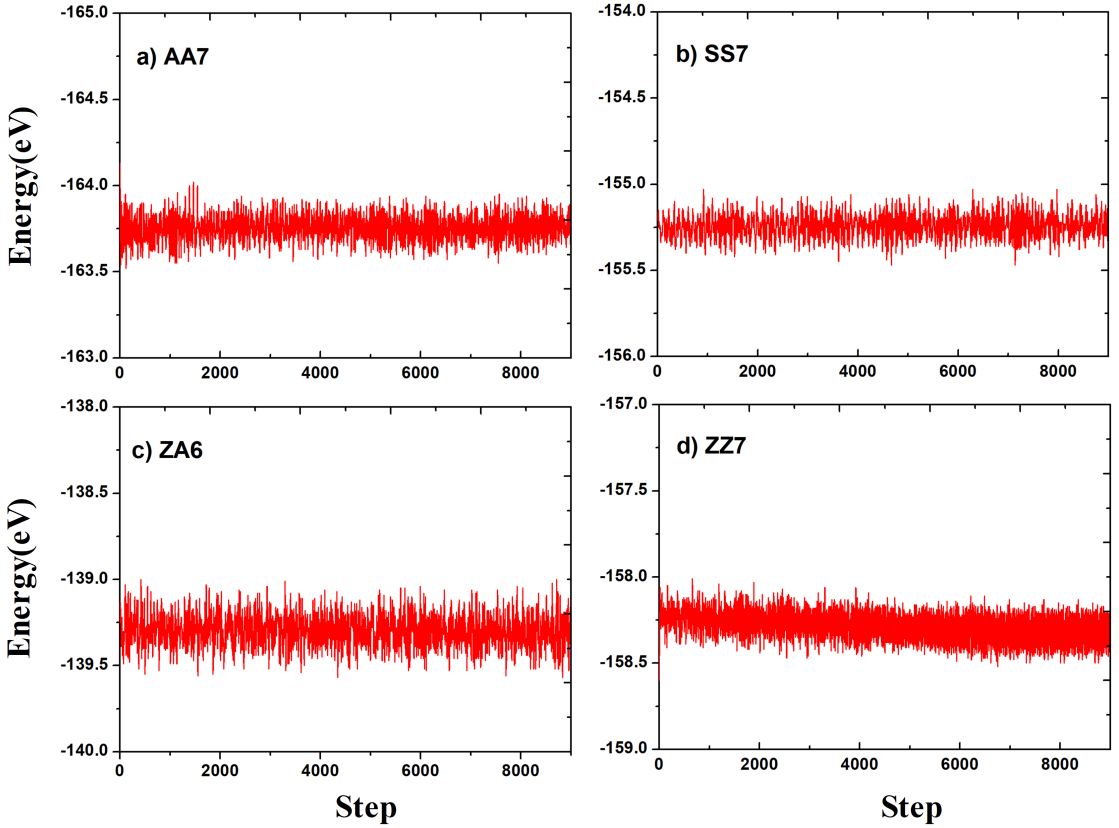

Fig. 3. Thermal stability plots for representative configurations of the four edge types of p-NiN_2NRs.

the spin down are at the ZA6 and ZA10. For the ZZ-p-NiN_2 structures, their bandgap exhibits a relatively complex dependence on the ribbon width, as displayed in Fig. 4(d), in which the highest and smallest bandgaps for spin up (black line) and spin down (red line) are at the ZZ13 and ZZ7 structures, respectively. Besides, the bandgaps of the spin down are larger than that of the spin up, regardless of any widths. It is worthy to note that the edge shapes strongly affect to the bandgap variation as well as their electronic properties.

Furthermore, the electronic band structures and density of states (DOS) of the penta NiN_2 nanoribbons with various edges and widths, the only tool to analyze their electronic properties, are presented in Fig. 5 for AA and SS edges and Fig. 6 for ZA and ZZ edges, whereas the Fermi level is set at zero energy to distinguish the valence and conduction states illustrated by the dashed green line. The spin polarization/magnetism and atom domination are analyzed by the spin splitting in electronic band structure/asymmetric peaks in DOS and atom (Ni, N, and H)-projected DOS (PDOS). Particularly, the spin splitting electronic band structure and PDOS are arranged at the left-hand side and right-hand side of Fig. 5 and Fig. 6, respectively, in which the spin up and spin down bands are illustrated by the black and red lines as well as positive and negative values

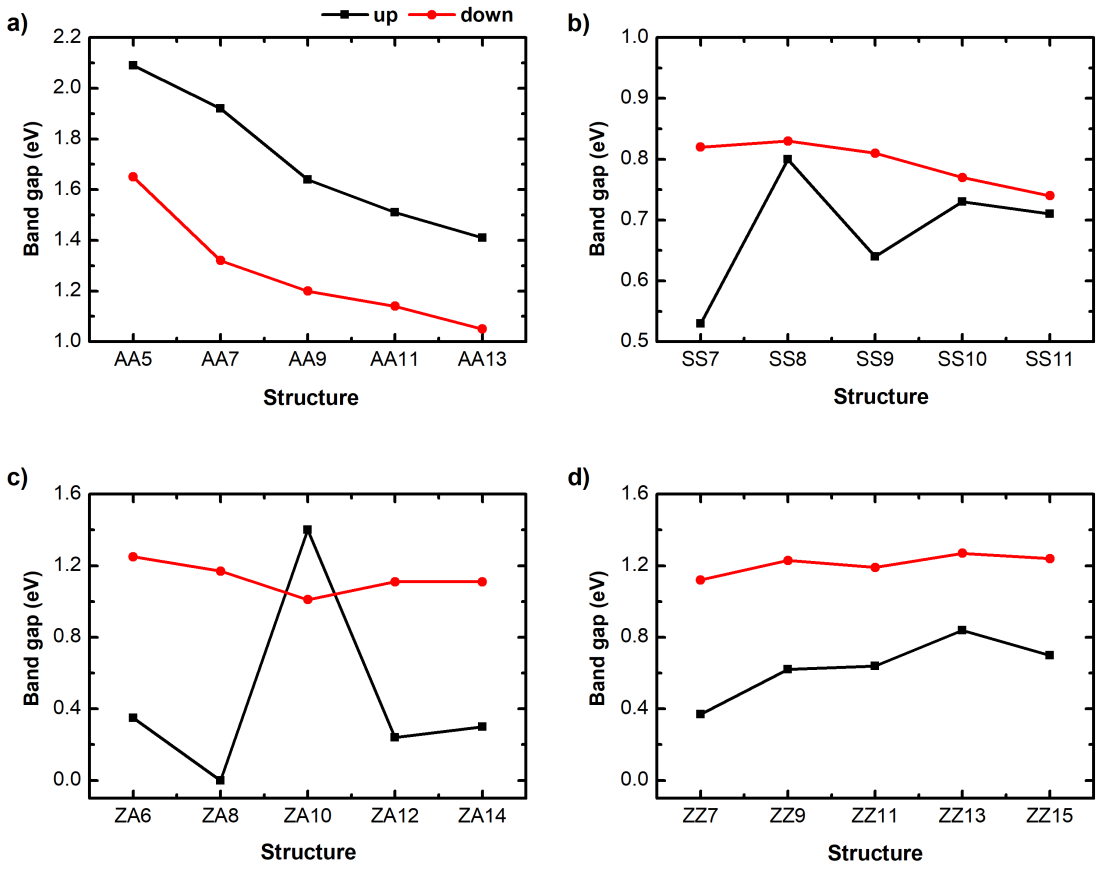

Fig. 4. (Color online) The bandgap variation for the four edge types of p-NiN_2NRs.

in PDOS. Besides, the values of bandgaps and magnetic moments are reported Table 1 and Table 2. As a result, all penta NiN_2 nanoribbons exhibit spin polarization that accompanies with significant net magnetic moments in range of 1.958 μ_B to 4.005 μ_B dependent on specific edges and widths, as identified by the significant spin splitting bands and asymmetric peaks via Fermi level in PDOS. Notably, the difference in magnetic moments between the sawtooth-sawtooth (SS) structure ($\sim$2.0 μ_B) and the other configurations (ZZ, ZA, and AA, all $\sim$4.0 μ_B) highlights the rich diversity of magnetic states that can be achieved through different edge terminations. It should note that the larger/smaller net magnetic moments are owing to higher/lower spin splitting in electronic band structures or more asymmetric/less asymmetric peaks in PDOS. Most of the penta NiN_2 nanoribbons behave as semiconductor that can observe via emerging the bandgap made of the highest occupied valence and lowest unoccupied conduction bands/states in band structure and PDOS. Especially, only the ZA8 structure displayed in Fig. 6(b) shows a half-metal that is ruled by existing a bandgap in spin down band (red line) and destroying a bandgap in spin up band (black line). It can determine that only the ZA8 structure belong to ferromagnetic half-metal and other ones are ferromagnetic semiconductors. This is different from penta graphene nanoribbon,

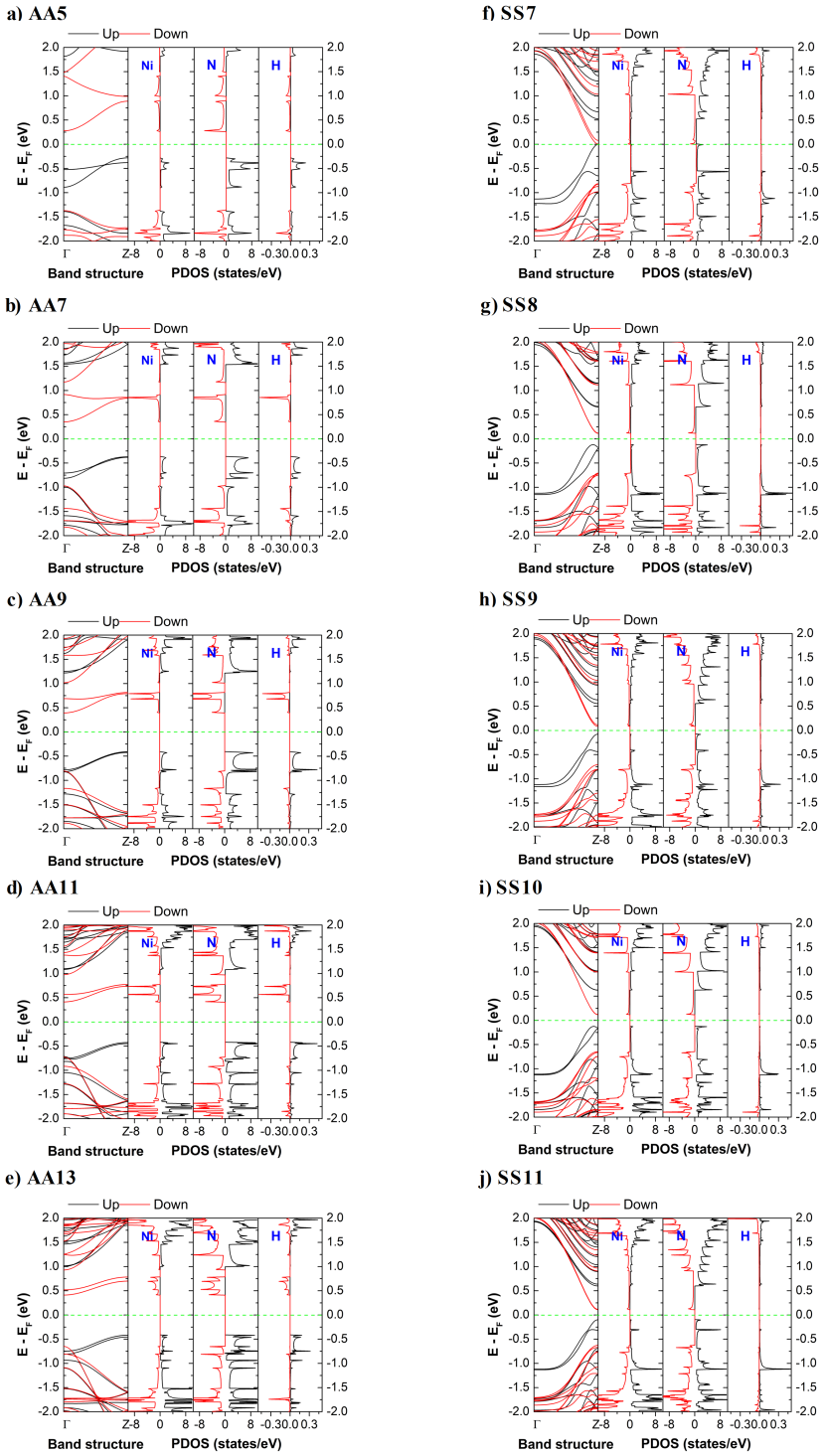

Fig. 5. (Color online) Spin-splitting band structure and atom-projected density of states (PDOS) for the AA and SS edge shapes of the p-NiN_2NRs with differrent widths.

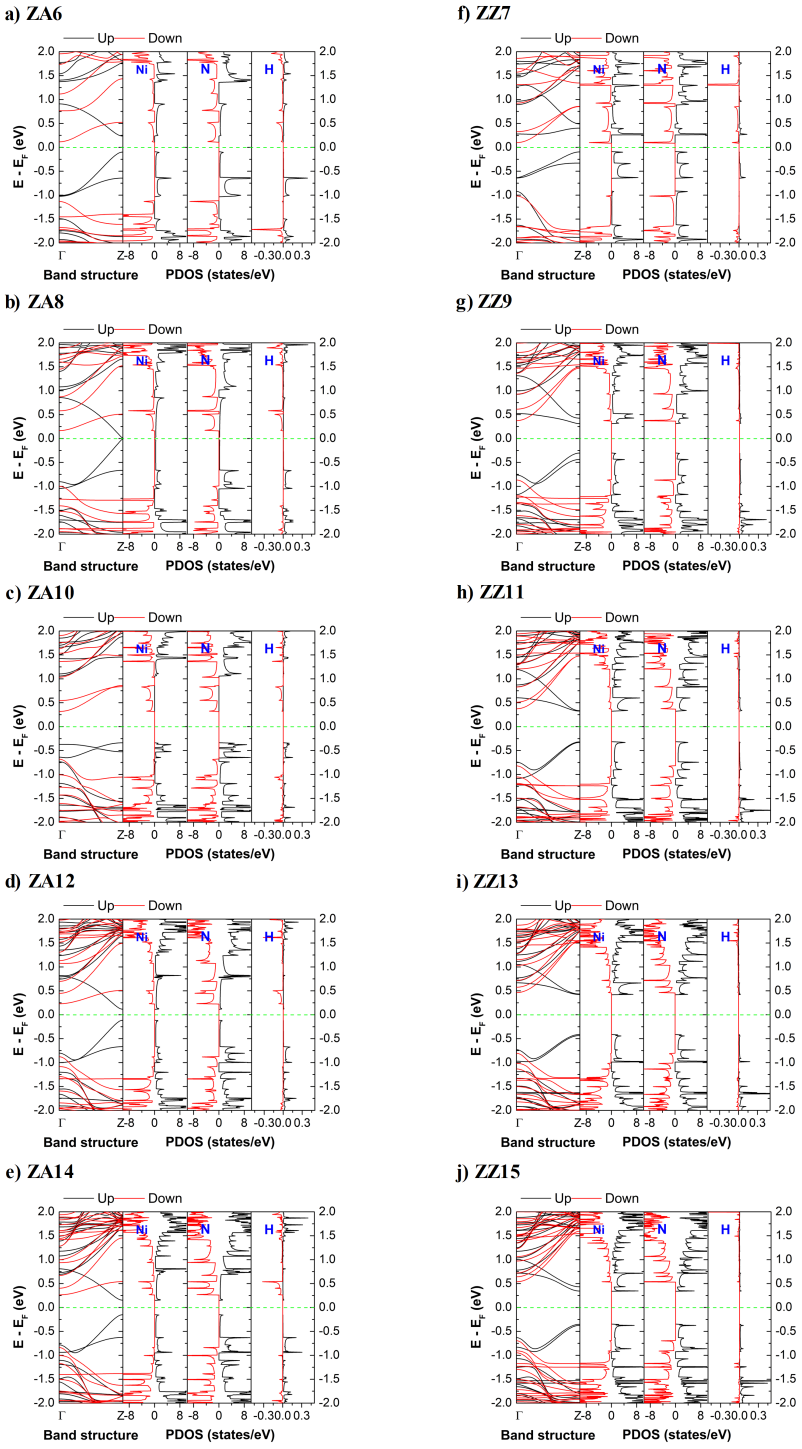

Fig. 6. (Color online) Spin-splitting band structure and atom-projected density of states (PDOS) for the ZA and ZZ edge shapes of the p-NiN_2NRs with different widths.

Table 1. Band gap [E_g (eV)]/metallic, net magnetic moment [$M(\mu_B)$], and magnetic-electronic characteristics of the studied structures.

Configurations	E_g (eV)/metallic	M(μ_B)	Characteristics
AA5	spin up: 2.09 (indirect)		
	spin down: 1.65 (direct)	4.005	semiconductor
AA7	spin up: 1.92 (indirect)		
	spin down: 1.32 (direct)	4.005	semiconductor
AA9	spin up: 1.64 (indirect)		
	spin down: 1.20 (direct)	4.005	semiconductor
AA11	spin up: 1.51 (indirect)		
	spin down: 1.14 (direct)	4.005	semiconductor
AA13	spin up: 1.41 (indirect)		
	spin down: 1.05 (direct)	4.005	semiconductor
SS7	spin up: metallic		
	spin down: metallic	1.958	semiconductor
SS8	spin up: 0.80 (indirect)		
	spin down: 0.83 (direct)	2.001	semiconductor
SS9	spin up: 0.64 (direct)		
	spin down: 0.81 (direct)	1.998	semiconductor
SS10	spin up: 0.73 (indirect)		
	spin down: 0.77 (direct)	2.001	semiconductor
SS11	spin up: 0.71 (direct)		
	spin down: 0.74 (direct)	2.000	semiconductor

SS-p-NiN_2 also exhibits strong spin polarization, while SS-penta graphene has no spin polarization [11]. In addition, ZZ-penta graphene, ZA-penta graphene, and AA-penta graphene are metallic, the p-NiN_2NRs with corresponding edge shapes exhibit semiconducting or half-metallic behavior depending on the specific width (ZA8).

On the magnetic aspect, to clarify the origin of net magnetic moments as well as the spin-splitting bands and spin asymmetric PDOS, the spatial spin density distributions are presented in Fig. 7, whereas the pink and cyan isosurfaces represent spin-up and spin-down states, respectively. The correlation in spin up and spin down states result in a net magnetic moments, whereas the positive/negative net magnetic moments are responsible with the more domination of spin up/spin down states. In Fig. 7, it is evident that the more spin up states dominate in the spin density distribution that leads to the positive net magnetic moments in all investigated structures, as indicated by the dominated pink isosurfaces. In contrast, spin-down contributions, shown in cyan, are minimal. Furthermore, as the chain width increases, the net magnetic moments become increasingly localized at the edges of the structures. Conversely, in narrower chains, the magnetic moments extend into the central region. For edge configurations labeled AA, ZZ, and ZA, the spin density exhibits a symmetric distribution along both edges, adhering to an odd-even rule in magnetic moment behavior. This trend is consistent with the results from band structure and density of states analyses. These findings highlight a significant impact of edge shapes and widths on

Table 2. Band gap [E_g (eV)]/metallic, net magnetic moment [$M(\mu_B)$], and magnetic-electronic characteristics of the studied structures.

Configurations	E_g (eV)/metallic	M(μ_B)	Characteristics
ZA6	spin up: 0.35 (direct)		
	spin down: 1.25 (direct)	4.002	semiconductor
ZA8	spin up: metallic		
	spin down: 1.17 (direct)	4.004	half metal
ZA10	spin up: 1.40 (indirect)		
	spin down: 1.01 (direct)	4.005	semiconductor
ZA12	spin up: 0.24 (direct)		
	spin down: 1.11 (direct)	4.005	semiconductor
ZA14	spin up: 0.30 (direct)		
	spin down: 1.11 (direct)	4.005	semiconductor
ZZ7	spin up: 0.37 (indirect)		
	spin down: 1.12 (direct)	4.000	semiconductor
ZZ9	spin up: 0.62 (direct)		
	spin down: 1.23 (direct)	4.005	semiconductor
ZZ11	spin up: 0.64 (direct)		
	spin down: 1.19 (direct)	4.005	semiconductor
ZZ13	spin up: 0.84 (direct)		
	spin down: 1.27 (direct)	4.005	semiconductor
ZZ15	spin up: 0.70 (direct)		
	spin down: 1.24 (direct)	4.005	semiconductor

electronic conduction with spin-polarized current and conduction predominantly occurring at the edges in ribbon-like structures [38–40].

Furthermore, the absorption coefficients of all the investigated samples derived from the real and imaginary parts of the dielectric functions are utilized to study the optical characteristic, as shown in Fig. 8. In general, with an increase in width, the major peaks of the absorption spectra are red-shifted toward lower energy regimes and the main peaks appear only in the Oy or Oz directions, as illustrated by blue and magneta curves in Fig. 8. While the p-AA-NiN_2, p-ZA-NiN_2 and p-ZZ-NiN_2 structures are sensitive in the visible light range (400 nm - 600 nm), the p-SS-NiN_2 structure stands out as excellent optical traps in the infrared region with the main peak corresponding to the wavelength of about 1000 nm. For the p-ZA-NiN_2 and p-ZZ-NiN_2 structures, the main peak in the Oz direction corresponds to the small width, and as the width increases, the main peak appears in the Oy direction. In contrast, the main peak always appears in the Oz direction for p-SS-NiN_2, while the p-AA-NiN_2 structure with a width of 13 will have a shift of the main peak from the Oz to the Oy direction. Specifically, in the case of p-AA-NiN_2, in the Oz direction, the wavelength of the main absorption peak becomes larger as the width increases due to the reduced electronic bandgap, while the main peak in the Oy direction fluctuates slightly around 320 nm. Similarly, the main peaks of the SS structures in the Oy and Oz directions fluctuate slightly around 300 nm and 1000 nm. For the p-ZA-NiN_2 and p-ZZ-NiN_2 structures, the main peak appears in the Oz direction at about 500 nm when the width is less than 10. The main peak

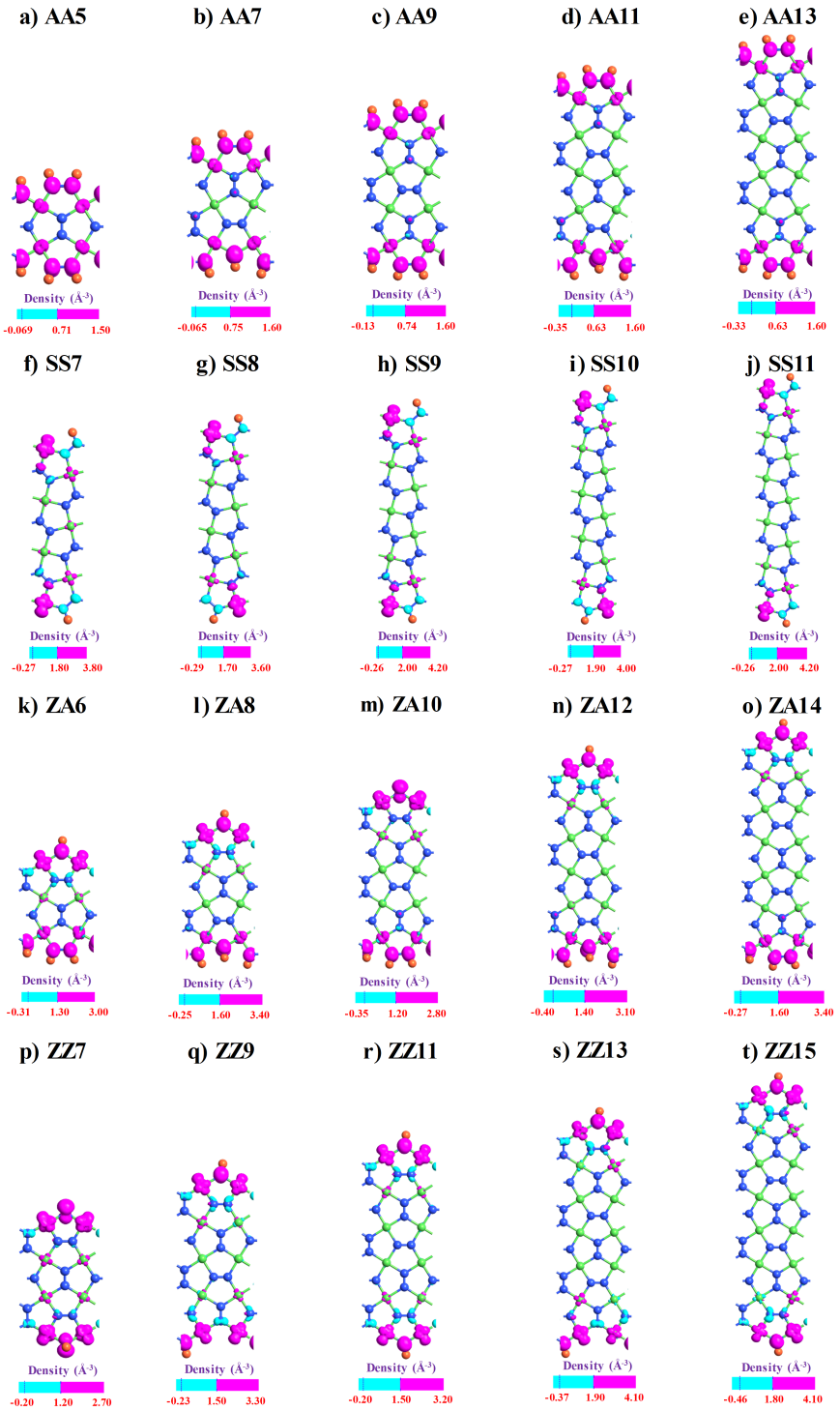

Fig. 7. (Color online) Spatial spin density distributions of p-NiN_2NRs, whereas pink and cyan isosurfaces represent for the spin up and spin down density distributions, respectively.

observed in the Oy direction is approximately 600 nm when the width increases. The results show that the absorption spectral region can be controlled by the widths and edge shapes for the penta NiN_2 nanoribbon structure that will be useful to develop practical applications for optoelectronic and photovoltaic fields.

3.3. Electronic transport properties

Fig. 9 shows the device model, are constructed by AA7-p-NiN_2, SS7-p-NiN_2, ZA6-p-NiN_2 and ZZ7-p-NiN_2. These device models are named DAA7, DSS7, DZA6, and DZZ7, respectively. As a result, the I-V characteristics of four devices constructed from penta NiN_2 nanoribbons with four different edge shapes are shown in Fig. 10, in which the red square and blue dot symbols represent for sin-up and spin-down current, respectively. The difference in I-V characteristics for the spin-up and spin-down states of the DAA7, DSS7, and DZA6 are clearly observed in Fig. 10(a), 10(b), and 10(c), respectively. In contrast, there is almost no difference in I-V characteristics for the two spin states for DZZ7, as shown in Fig. 10(d). The two prominent features for the I-V spectra of the DAA7, DSS7, and DZA6 are the negative differential characteristics and the spin filtering efficiency.

Specifically, the I-V curve for DAA7 in Fig. 10(a) shows the spin-up (red square symbol) current with the current peaks emerging at approximately 2.4 μA at a very low potential of 0.1 V, then gradually decreasing to zero over the range of 0.1 V – 0.8 V, and increasing slightly over the range of 0.9 V – 1.0 V. In the negative bias, the spin-up current peaks at approximately 1.8 μA at -0.1 V, gradually decreasing to 0 μA in the negative bias range of -0.2 V to -1.0 V. Negative differential characteristics, spin-filtering efficiency, and spin separation over the range of -0.2 V to 0.2 V are obtained for this sample. The current intensity reaches a maximum at $\pm$0.1 V and decreases rapidly to 0 μA at a potential of $\pm$0.2 V, the negative differential ratio for the spin-up and spin-down states is about 10^5, respectively. The spin filtering efficiency at the potential point of $\pm$0.1 V also reaches 99%. The spin splitting for the potential range of $\pm$0.2 V with the maximum current intensity of the spin-up state, on the other hand, the spin-down state has a negligible current intensity. Meanwhile, the spin splitting around the bias range from 0.2 V to 0.4 V or -0.2 V to -0.4 V is less pronounced with the current intensity in the two spin states following the opposite trend.

The I-V curve for the DSS7 is shown in Fig .10(b). For the spin-up current, the current quickly reaches a maximum at $\pm$0.1 V, tends to decrease to 0 μA when the voltage is in the range [$\pm$0.1 V, $\pm$0.7 V]. Therefore, the negative differential resistance characteristic is clearly shown in this voltage range. The corresponding negative differential ratios for the positive and negative bias are about 20 and 30. In the remaining bias range [$\pm$0.7 V, $\pm$1.0 V], the current increases slightly. For the spin-down current, the current after reaching a maximum at $\pm$0.1 V, gradually decreases to 0 μA, maintains at 0 μA in the bias range [$\pm$0.3 V; $\pm$0.8 V], and then increases gradually to about 5 μA at $\pm$1.0 V. The negative differential ratio in this state is in the bias range [$\pm$0.1 V, $\pm$0.3 V] is around 50. The spin filter efficiency for DSS7 also reaches 98% at the $\pm$0.3 V bias point and fluctuates slightly around this value at $\pm$0.4 and $\pm$0.5 V.

Similar to DAA7 and DSS7, the spin-up current of DZA6 shown in Fig. 10(c) rapidly reaches a maximum at $\pm$0.1 V. The maximum current remains in the range [$\pm$0.1, $\pm$0.3], and the current decreases sharply as the bias approaches $\pm$0.5 V. The DZA6 current exhibits high symmetry in both positive and negative biases for the [0, $\pm$0.5] voltage range. When biasing from $\pm$0.5 V onward, the asymmetry for the I-V spectrum is clearly observed. For the positive bias,

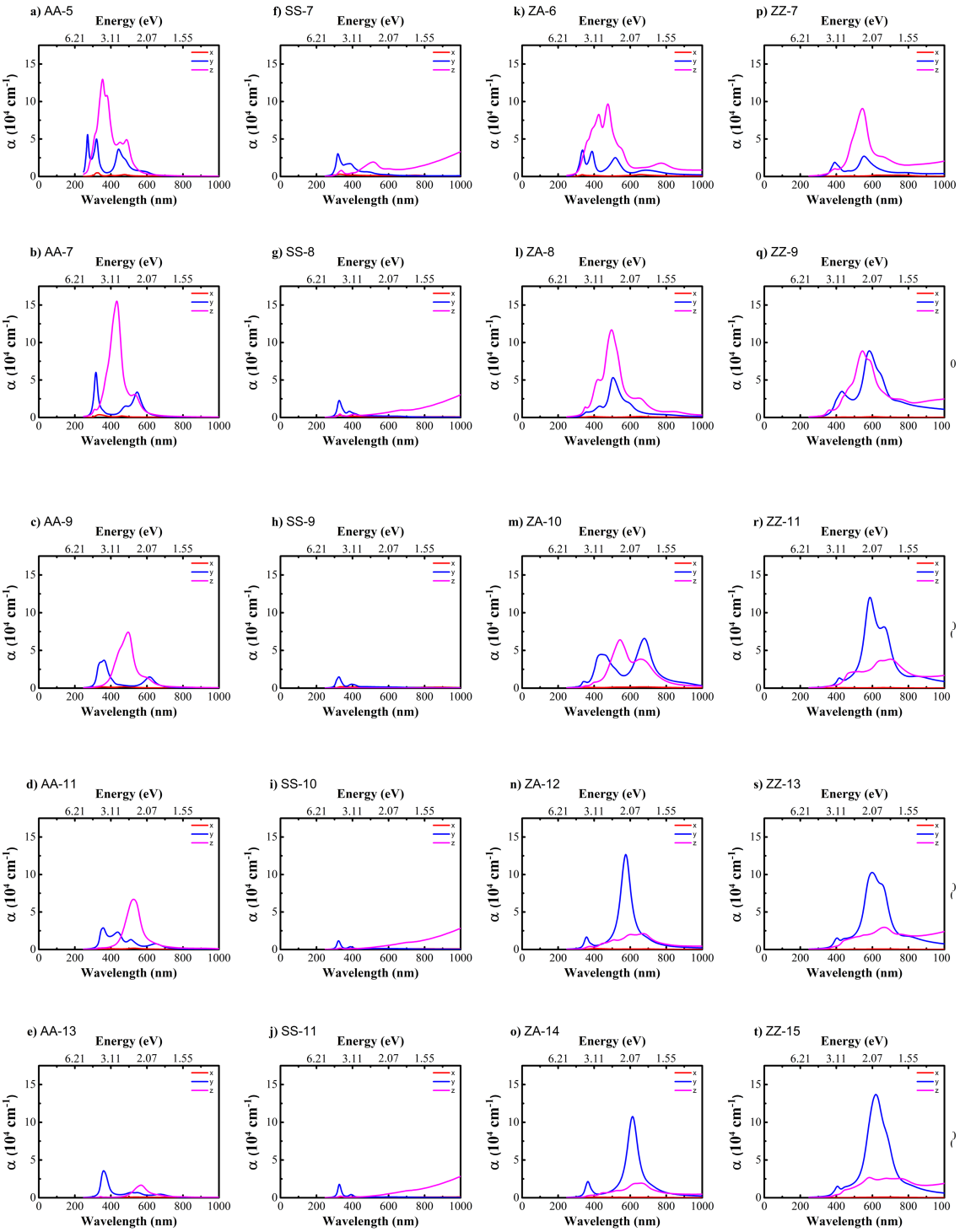

Fig. 8. Optical absorption spectra of four edge types of p-NiN_2NRs.

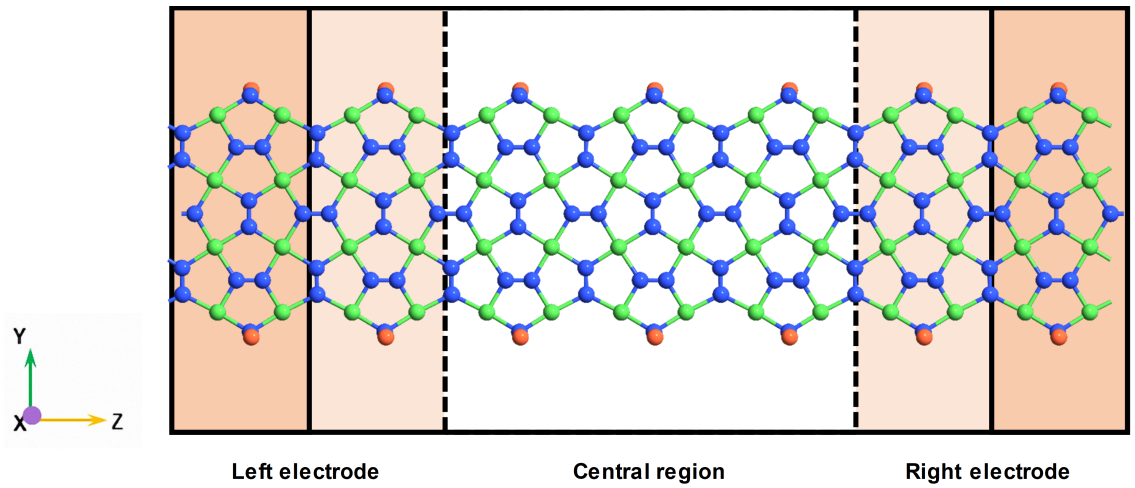

Fig. 9. Top-view model of the transport device. The green, blue, and orange balls represent Ni, N and H atoms, respectively.

after the current reaches its minimum at 0.5 V, it gradually increases as the bias changes from 0.5 V to 0.8 V, peaks at 0.8 V, reaches its second minimum at 0.9 V, and increases again as the bias increases to 1.0 V. Therefore, two negative differential points are observed for the spin-up state of DZA6 with positive bias at values around 4.2 and 2.5. Meanwhile, for the negative bias, after the current reaches its minimum at 0.5 V, it gradually increases at -0.6 V and maintains this value in the remaining bias range [-0.6, -1.0 V]. Spin-filtering efficiency above 60% is also obtained in the bias range [0,$\pm$0.4 V] for DZA6.

The morphology of the I-V curve for DZZ7 is completely different from the other three models, as observed in Fig. 10(d), whereas the current intensity is almost maintained at approximately 0 A in the bias range [-0.8 V; 0.8 V] for both spin-up and spin-down states, from this bias the current intensity value increases and reaches 7×10^{-5} μA and 44×10^{-5} μA at 1.0 V and -1.0 V. Thus, the negative differential effect and spin filtering efficiency have very low values in this model and are only observable on the nanoampere (nA) or picoampere (pA) scale.

In order to further understand the NDR effect in the systems, the transmission functions (T(E)) and the eigenstates of the DAA7, DSS7, DZA6, and DZZ7 samples for spin-up are investigated, as presented in Fig. 11(a), 11(b), 11(c), and 11(d), respectively, in which it is named as DAA7-up, DSS7-up, DZA6-up, and DZZ7-up. For DAA7-up in Fig. 11(a), in a small bias window [-0.05 V, 0.05 V], the T(E) ranges from 0 to 1.4 and peaks at 1.4. As a result, the current intensity reaches a maximum at 0.1 V. On the contrary, the magnitude T(E) is maintained almost 0 in bias window [-0.1 V, +0.1 V], so the current intensity at 0.2 V is approximately 0. Therefore, the ratio between the current intensity at bias 0.1 V and 0.2 V of DAA7-up reaches a very large value, approximately 10^5, demonstrating a strong negative differential effect. A similar trend is obtained in Fig. 11(b) for the DSS7-up at biases of 0.1 V and 0.7 V. The negative differential effect is less pronounced for the DZA6-up at biases of 0.3 V and 0.5 V, as identified in Fig. 11(c). At 0.3 V, the T(E) value reaches a maximum of 1, while at 0.5 V it is about 0.35. Therefore, the ratio between

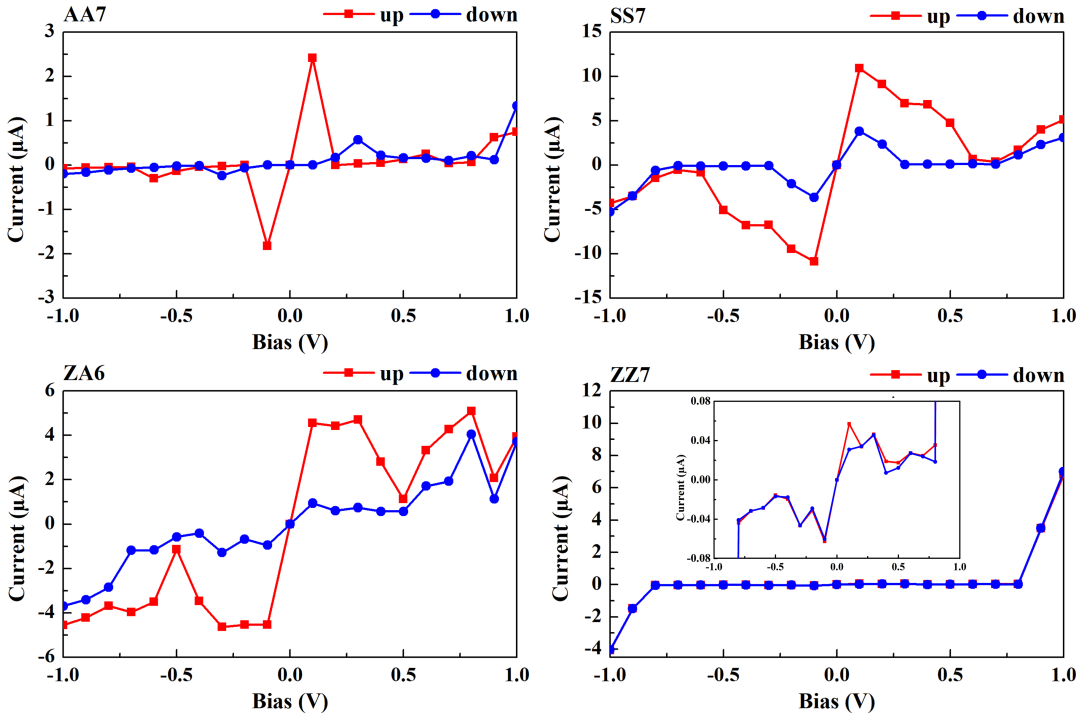

Fig. 10. (Color online) I–V characteristic curves of a) DAA7, b) DSS7, c) DZA6, d) DZZ7. The red square symbols represent spin-up currents. The blue dot symbols represent spin-down currents.

the maximum and minimum current in this voltage range is approximately 20, much lower than that of the DAA7-up and DSS7-up. As for the DZZ7-up in Fig. 11(d), it shows that the T(E) value of the DZZ7-up in the bias ranges [-0.4 V, 0.4 V] and [-0.5 V, 0.5 V] is almost zero. This explains the extremely low current value of the DZZ7-up.

The SF efficiency (SFE) is another prominent feature that has to take into account. In DAA7 configuration, the spin-up current increases linearly till $\pm$0.1 V, while the spin-down current has a 0 μA value within the voltage range of [-0.1 V, 0.1 V]. As a result, the SF effect can be observed. This shows that the spin-up electrons can move more easily from the left electrode to the right electrode within the voltage range of $[-0.1V, +0.1V]$. In contrast, the movement of the spin-down electrons almost prohibited in this bias range. A similar tendency is observed for DSS7. The spin-up electrons can move more easily from the left electrode to the right electrode within the voltage range of [$\pm$0.1 V, $\pm$0.5 V], while the movement of the spin-down electrons is almost prohibited. Therefore, the SF efficiency is observed very clearly in this voltage range. The SFE in DZA6 is observed within the voltage range of [$\pm$0.1 V, $\pm$0.4 V] with lower efficiency. DZZ7 does not exhibit SFE because the currents in the spin- up and spin-down states are similar throughout the bias point examined.

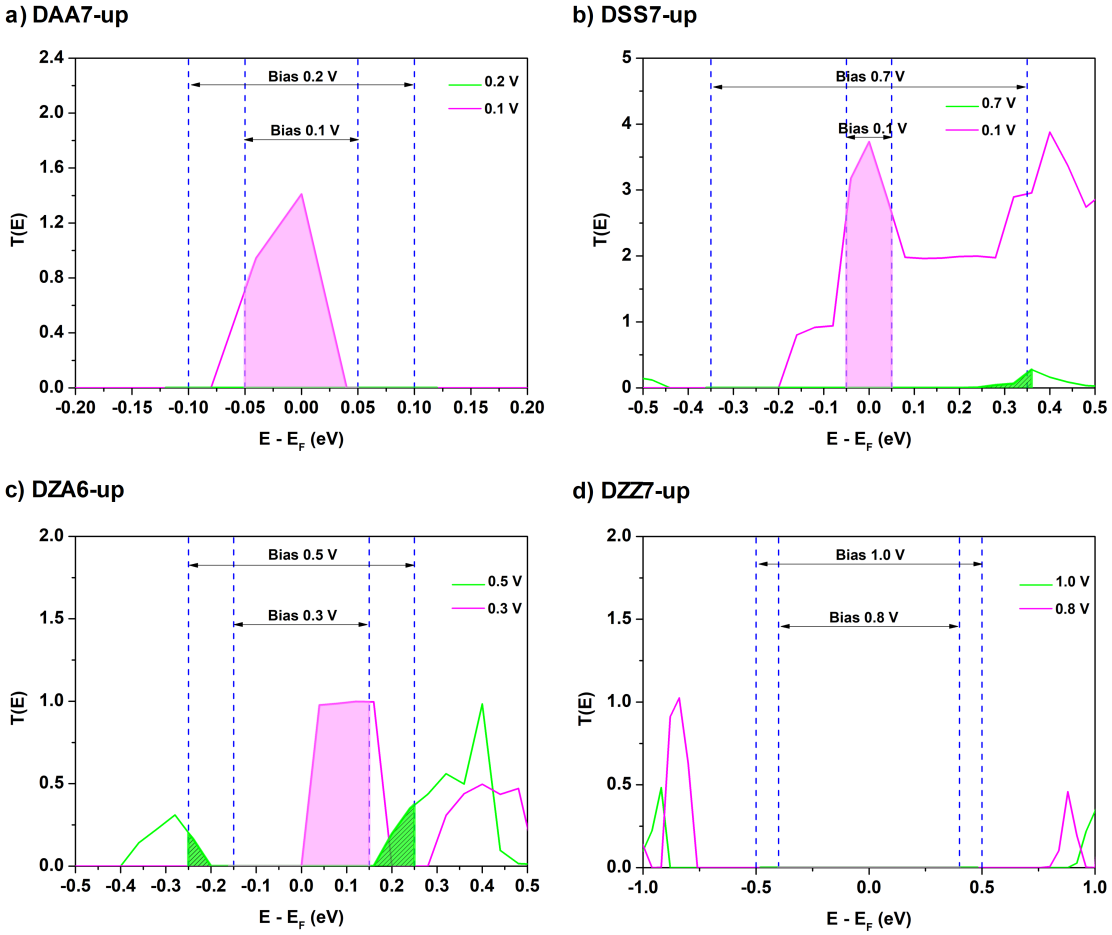

Fig. 11. Transmission functions of the ZZ-p-PdSe2NRs at special bias potential of a) DAA7-up, b) DSS7-up, c) DZA6-up, d) DZZ7-up.

The SF efficiency (SFE) is calculated by the following formula [41, 42],

$$SFE = (I_{up} - I_{down})/(I_{up} + I_{down}), \tag{7}$$

where the I_{up} and I_{down} are the current of spin-up and spin-down, respectively.

Fig. 12 shows the calculated spin filtering efficiency (SFE) of the four studied devices (DAA7, DSS7, DZA6, and DZZ7), in which the bias voltage range of [-1 V, 1 V]. The SFE reaches about 99% at $\pm$0.2 V for DAA7 system, while its value is about 98% at $\pm$0.3 V for DSS7. The SFE of both systems maintains a value of 90% in the voltage range [-0.5 V, 0.5 V] and decreases sharply as the voltage increases towards 1 V.The SFE of DZA6 fluctuates continuously between 10% and 80% in the bias range [-0.8 V, 0.8 V] and tends to decrease as the voltage increases to 1 V. For DZZ7, this effect is almost absent for negative bias, while the SFE reaches a maximum value of about 40% for positive bias.

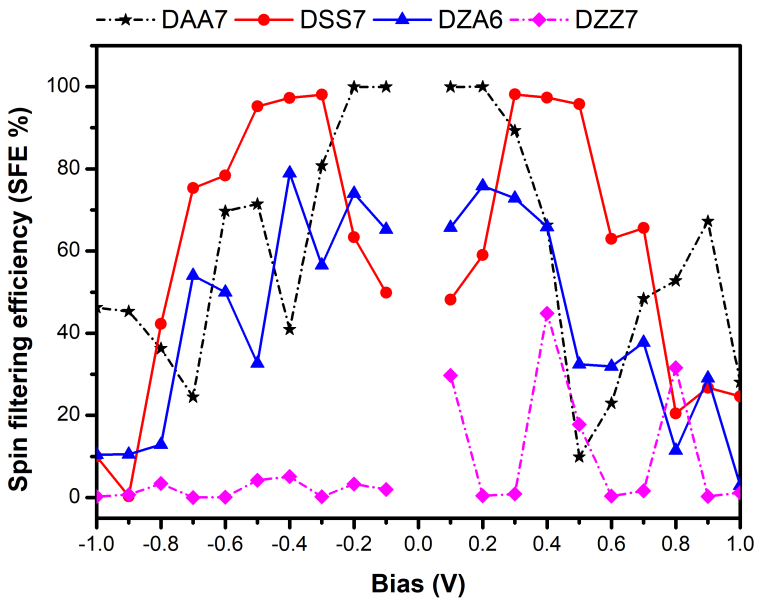

Fig. 12. Spin filtering efficiency (SFE) of four studied devices.

4. Conclusions

Using the DFT method with highly accurate hybrid functional (HSE06), the structural, electronic, optical, and electronic transport properties of the p-NiN_2 nanoribbons with four typical edge shapes of armchair–armchair, sawtooth–sawtooth, zigzag–armchair, and zigzag–zigzag are fully revealed, in which their various widths are included that leads to 20 different optimal configurations. The key quantities have been developed to analyze the structural, electronic, optical, and electronic transport properties of the studied configurations include the binding energies, thermal stability, spin-splitting electronic band structures, atom-projected density of states, spatial spin density distribution, optical absorption spectra, I-V curves, transmission functions (T(E)), and spin filtering efficiency. The p-NiN_2NR systems achieve a good structural stability as evidenced by their significant negative formation energies in range of -6.1 eV to -7.0 eV, whereas the SS edge shape possesses the highest stability among other ones. This finding is further corroborated by their excellent thermal stability, confirmed via AIMD simulations that showed only minor fluctuations in total energy, well within a narrow range of approximately 0.5 eV. On the electronic characteristics, only the ZA8 configuration behaves as ferromagnetic half-metal as determined by remaining a bandgap in spin-down bands and destroying a bandgap in spin-up bands in its spin-splitting electronic band structure. In contrast, other configurations all belong to ferromagnetic semiconductors as determined by emerging the spin-splitting bandgaps in their spin-splitting electronic band structures. On the magnetic aspect, the origin of the significant net magnetic moments as well as the spin splitting in band structures is clarified by the spatial spin density distribution, in which the spin-up states show stronger domination than the spin-down states, resulting in the positive net magnetic moments. As for optical absorption spectra of the penta NiN_2 nanoribbon, it

indicates that the absorption spectral region can be sensitively controlled by the widths and edge shapes. As analyzing in the I-V spectra, it indicates that the negative differential characteristics and the spin filtering efficiency appear in the DAA7, DSS7, and DZA6 configurations, and only disappear in the DZZ7 configuration. The transmission function (T(E)) of the DAA7-up and the DSS7-up configurations shows stronger negative differential effect than that of the the DZA6-up and DZZ7-up configurations. In addition, the spin filtering efficiency (SFE) of the DAA7 and DSS7 configurations are much higher than that of DZA6 and DZZ7. The essential electronic, optical, and electronic transport properties of the p-NiN_2 nanoribbons controlled by edge shapes and widths are very potential for next-generation electronic, optoelectronic, and spintronic applications.

Acknowledgements

This research is funded by Vietnam National Foundation for Science and Technology Development (NAFOSTED) under Grant No. 103.01-2023.06. The calculations were carried out on the Can Tho University (MOMA Lab) high-performance computing facilities and the NatSciDP group.

Authors contributions

Nguyen Hai Dang: Conceptualization, investigation, data curation, methodology, formal analysis, visualization, writing - original draft. Pham Thi Bich Thao, Thai Van Thanh: Investigation, data curation, visualization, writing - review and editing. Nguyen Thanh Tien: Supervision, investigation, visualization, formal analysis, writing-review and editing.

Conflict of interest

The authors have no conflicts to disclose.

References

[1] M. J. Molaei, M. Younas and M. Rezakazemi, *A comprehensive review on recent advances in two-dimensional (2d) hexagonal boron nitride*, ACS Appl. Electron. Mater. **3** (2021) 5165.

[2] S. Jana, A. Bandyopadhyay, S. Datta, D. Bhattacharya and D. Jana, *Emerging properties of carbon based 2D material beyond graphene*, J. Phys.: Condens. Matter **34** (2021) 053001.

[3] S. Zhang, J. Zhou, Q. Wang, X. Chen and Y. Kawazoe, *Penta-graphene: A new carbon allotrope*, Proc. Natl. Acad. Sci. U.S.A. **112** (2015) 2372.

[4] Y. Ying, K. Fan, X. Luo and H. Huang, *Predicting two-dimensional pentagonal transition metal monophosphides for efficient electrocatalytic nitrogen reduction*, J. Mater. Chem. A **7** (2019) 11444.

[5] Y. Guo, J. Zhou, H. Xie, Y. Chen and Q. Wang, *Screening transition metal-based polar pentagonal monolayers with large piezoelectricity and shift current*, npj Comput. Mater. **8** (2022) 40.

[6] L. Liu, B. Jiang, D. Sun, H. Liu and Y. Xie, *Ab initio high-throughput screening of transition metal double chalcogenide monolayers as highly efficient bifunctional catalysts for photochemical and photoelectrochemical water splitting*, J. Mater. Chem. A **10** (2022) 14060.

[7] A. Lopez-Bezanilla and P. B. Littlewood, *σ–π-band inversion in a novel two-dimensional material*, J. Phys. Chem. C **119** (2015) 19469.

[8] A. Bafekry, M. Faraji, M. M. Fadlallah, H. R. Jappor and N. N. Hieu, *Ab-initio-driven prediction of puckered penta-like PdPSeX (X = O, S, Te) janus monolayers*, Appl. Surf. Sci. **582** (2022) 152356.

[9] K. Zhao, Y. Guo, Y. Shen, Q. Wang and Y. Kawazoe, *Penta-bcn: A new ternary pentagonal monolayer with intrinsic piezoelectricity*, J. Phys. Chem. Lett. **11** (2020) 3501.

[10] K. Zhao, X. Li, S. Wang and Q. Wang, *2D planar penta-MN_2 (M = Pd, Pt) sheets identified through structure search*, Phys. Chem. Chem. Phys. **21** (2019) 246.
[11] J.-H. Yuan, Y.-Q. Song, Q. Chen, K.-H. Xue and X.-S. Miao, *Single-layer planar penta-X_2N_4 (X = Ni, Pd and Pt) as direct-bandgap semiconductors*, Appl. Surf. Sci. **469** (2019) 456.
[12] H. Wang, Z. Chen and Z. Liu, *Penta-CN_2 revisited: Superior stability, synthesis condition exploration, negative poisson's ratio and quasi-flat bands*, Appl. Surf. Sci. **585** (2022) 152536.
[13] X. Li, F. Zhang, J. Li, Z. Wang, Z. Huang, J. Yu *et al.*, *Pentagonal C_m X_n Y_{6-m-n} (m = 2, 3; n = 1, 2; X, Y = B, N, Al, Si, P) monolayers: Janus ternaries combine omnidirectional negative poisson ratios with giant piezoelectric effects*, J. Phys. Chem. Lett. **14** (2023) 2692.
[14] B. R. Sharma, A. Manjanath and A. K. Singh, *Pentahexoctite: A new two-dimensional allotrope of carbon*, Sci. Rep. **4** (2014) 7164.
[15] S. Winczewski and J. Rybicki, *Anisotropic mechanical behavior and auxeticity of penta-graphene*, Carbon **146** (2019) 572.
[16] S. B. Sharma, I. A. Qattan, S. Kc and A. M. Alsaad, *Large negative poisson's ratio and anisotropic mechanics in new penta-PBN monolayer*, ACS Omega **7** (2022) 36235.
[17] W. Lei, S. Zhang, G. Heymann, X. Tang and J. Wen, *A new 2D high-pressure phase of $PdSe_2$ with high-mobility transport anisotropy for photovoltaic applications*, J. Mater. Chem. C **7** (2019) 2096.
[18] M. Bykov, E. Bykova, A. V. Ponomareva, F. Tasnadi and S. Chariton, *Realization of an ideal cairo tessellation in nickel diazenide nin2*, ACS Nano **15** (2021) 13539.
[19] R. Duan, C. Zhu, Q. Zeng, X. Wang and Y. Gao, *Pdpse: Component-fusion-based topology designer of two-dimensional semiconductor*, Adv. Funct. Mater. **31** (2021) 2102943.
[20] P. Li, J. Zhang, C. Zhu, W. Shen and C. Hu, *Penta-PdPSe: A new 2D pentagonal material with highly in-plane optical, electronic, and optoelectronic anisotropy*, Adv. Mater. **33** (2021) 2102541.
[21] R. Duan, Y. He, C. Zhu and X. Wang, *2D cairo pentagonal PdPS: Air-stable anisotropic ternary semiconductor with high optoelectronic performance*, Adv. Funct. Mater. **32** (2022) 2113255.
[22] Y. Hu, X. Zhao, Y. Yang, W. Xiao and X. Zhou, *Coordination engineering on novel 2D pentagonal NiN_2 for bifunctional oxygen electrocatalysts*, Appl. Surf. Sci. **614** (2023) 156256.
[23] D.-Y. Sun, L.-H. Li, G.-T. Yuan, Y.-L. Ouyang and R. Tan, *Enhanced oer catalytic activity of single metal atoms supported by the pentagonal NiN_2 monolayer*, Phys. Chem. Chem. Phys. **26** (2024) 6292.
[24] S. Wu, Q. Xie and W. Shi, *First-principle prediction of penta-NiN_2 monolayer as electrode materials for na and k ion batteries*, Chem. Phys. Lett. **837** (2024) 141066.
[25] M. Mahmoudi, D. König, X. Tan and S. C. Smith, *Lithium intercalation in two-dimensional penta-NiN_2*, Nanoscale **16** (2024) 3985.
[26] M. Li and X.-F. Wang, *Adsorption behaviors of small molecules on two-dimensional penta-NiN_2 layers*, ACS Appl. Nano Mater. **6** (2023) 6151.
[27] B. Rajbanshi, S. Sarkar, B. Mandal and P. Sarkar, *Energetic and electronic structure of penta-graphene nanoribbons*, Carbon **100** (2016) 118.
[28] N. T. Tien, P. T. B. Thao, V. T. Phuc and R. Ahuja, *Electronic and transport features of sawtooth penta-graphene nanoribbons via substitutional doping*, Physica E **114** (2019) 113572.
[29] T. Y. Mi, N. D. Khanh, R. Ahuja and N. T. Tien, *Diverse structural and electronic properties of pentagonal SiC_2 nanoribbons: A first-principles study*, Mater. Today Commun. **26** (2021) 102047.
[30] N. T. Tien, P. T. B. Thao and N. D. Khanh, *Structural, magneto-electronic, and electric transport properties of pentagonal $PdSe_2$ nanoribbons: A first-principles study*, Surface Sci. **728** (2023) 122206.
[31] K. Stokbro and K. Kaasbjerg, *Semiempirical model for nanoscale device simulations*, Phys. Rev. B **82** (2010) 075420.
[32] S. Smidstrup and T. Markussen, *Quantumatk: An integrated platform of electronic and atomic-scale modelling tools*, J. Phys.: Condens. Matter **32** (2019) 015901.
[33] M. Quinten, *Optical properties of nanoparticle systems: Mie and beyond*. John Wiley & Sons, 2010.
[34] S. Maekawa and T. Shinjo, *Spin dependent transport in magnetic nanostructures*. CRC press, 2002.
[35] E. G. Emberly and G. Kirczenow, *Molecular spintronics: spin-dependent electron transport in molecular wires*, Chem. Phys. **281** (2002) 311.

[36] N. T. Tien, P. T. B. Thao, V. T. Phuc and R. Ahuja, *Electronic and transport features of sawtooth penta-graphene nanoribbons via substitutional doping*, Physica E **114** (2019) 113572.
[37] Z. Zhu, Z. H. Zhang, D. Wang, X. Q. Deng and Z. Q. Fan, *Magnetic structure and magnetic transport characteristics of nanostructures based on armchair-edged graphene nanoribbons*, J. Mater. Chem. C **3** (2015) 9657.
[38] Y.-W. Son, M. L. Cohen and S. G. Louie, *Half-metallic graphene nanoribbons*, Nature **444** (2006) 347.
[39] F.-b. Zheng, C.-w. Zhang, S.-s. Yan and F. Li, *Novel electronic and magnetic properties in N or B doped silicene nanoribbons*, J. Mater. Chem. C **1** (2013) 2735.
[40] N. T. Tien, P. T. B. Thao, V. T. Phuc and R. Ahuja, *Influence of edge termination on the electronic and transport properties of sawtooth penta-graphene nanoribbons*, J. Phys. Chem. Solids **146** (2020) 109528.
[41] N. Taghizade and E. Faizabadi, *Spin-filtering effects and negative differential resistance in N/B-doped zigzag silicon carbide nanoribbons with asymmetric edge hydrogenation*, Mater. Sci. Eng. B **271** (2021) 115253.
[42] X. Cui and J. Li, *Multifunctional spintronic device based on zigzag SiC nanoribbon heterojunction via edge asymmetric dual-hydrogenation*, Physica E **138** (2022) 115253.